Cellular resolution optical access to brain regions in fissures: Imaging medial prefrontal cortex and grid cells in entorhinal cortex

Ryan J. Low[a,b,1], Yi Gu[a,b,1], and David W. Tank[a,b,c,2]

[a]Princeton Neuroscience Institute, [b]Bezos Center for Neural Circuit Dynamics, and [c]Department of Molecular Biology, Princeton University, Princeton, NJ 08544

In vivo two-photon microscopy provides the foundation for an array of powerful techniques for optically measuring and perturbing neural circuits. However, challenging tissue properties and geometry have prevented high-resolution optical access to regions situated within deep fissures. These regions include the medial prefrontal and medial entorhinal cortex (mPFC and MEC), which are of broad scientific and clinical interest. Here, we present a method for in vivo, subcellular resolution optical access to the mPFC and MEC using microprisms inserted into the fissures. We chronically imaged the mPFC and MEC in mice running on a spherical treadmill, using two-photon laser-scanning microscopy and genetically encoded calcium indicators to measure network activity. In the MEC, we imaged grid cells, a widely studied cell type essential to memory and spatial information processing. These cells exhibited spatially modulated activity during navigation in a virtual reality environment. This method should be extendable to other brain regions situated within deep fissures, and opens up these regions for study at cellular resolution in behaving animals using a rapidly expanding palette of optical tools for perturbing and measuring network structure and function.

two-photon imaging | medial prefrontal cortex | medial entorhinal cortex | grid cell

Optical tools provide powerful means to measure and perturb the structure and function of neural circuits (1). However, a key set of brain regions remains outside the reach of cellular-resolution optical methods: those situated within deep fissures. In the rodent brain, these areas include the medial prefrontal and medial entorhinal cortex (mPFC and MEC), two of the most widely studied regions supporting cognitive functions. The mPFC is centrally important to planning, executive function, learning, and memory (2, 3). Understanding how the mPFC implements these functions at a mechanistic, circuit level remains a longstanding goal of the field. The entorhinal cortex forms the interface between the neocortex and hippocampus and is believed to play an essential role in episodic memory and spatial information processing. These functions are particularly associated with MEC grid cells, which fire on a hexagonal lattice as an animal moves through an environment (4). Grid cells have galvanized a large body of work investigating their computational role and the mechanisms underlying grid formation, which remain important, open questions (4, 5). Moreover, mPFC or MEC dysfunction is associated with addiction, depression, schizophrenia, Alzheimer's disease, and epilepsy.

The study of the mPFC, MEC, and neighboring regions could be greatly advanced by in vivo, high-resolution optical tools. However, tissue properties and geometry present significant challenges to deploying these tools within deep fissures. For example, the depth of two-photon microscopy is limited by scattering and out-of-plane excitation (6). Access in the mammalian brain is therefore typically restricted to superficial regions (<500 μm with commonly used lasers, optics, and fluorescent labeling strategies). In contrast, the mPFC and MEC continue

deeper than 1 mm below the dorsal surface of the brain (Fig. 1*A*) (7). Furthermore, the mPFC and MEC are oriented vertically along the walls of deep fissures (the longitudinal and transverse fissures, respectively), and lie folded against the opposing walls (Fig. 1*A*). This geometry constrains approach angles and could induce wavefront aberrations in certain imaging configurations. Anatomical features of the vasculature and meninges surrounding fissures also present unique challenges. In particular, dural venous sinuses and associated vasculature, which form one of the major venous outflow systems of the brain, course over the fissures and block access to the underlying tissue (8).

Here, we present a general method for in vivo, two-photon imaging of brain regions situated within deep fissures. Our approach involves inserting a right angle microprism into the fissure, which bends the optical path within the brain by 90° and provides optical access to the fissure wall with subcellular resolution and a field of view suitable for large-scale recording (Fig. 1*B*). In dorsal cortical regions, microprisms were previously inserted directly into the brain tissue to image multiple cortical layers (9–11). Here, we developed methodology enabling the use of microprisms in a different configuration for optically accessing brain regions that have plunged vertically to form the walls of deep fissures.

We imaged the mPFC and MEC in head-fixed mice running on a spherical treadmill, and performed chronic recordings over multiple weeks. We recorded structural images using fluorescent marker proteins and measured network activity at cellular

Significance

High-resolution optical tools provide unprecedented capabilities for probing brain function in behaving animals, but require the ability to deliver and collect light to and from the brain with high spatial precision. This has proven challenging in regions within deep fissures in the brain, including the medial prefrontal and medial entorhinal cortex (mPFC and MEC), which are of broad scientific and clinical interest. We developed a general method for optical access to brain regions situated within deep fissures, and demonstrate its use in the mPFC and MEC by optically measuring the activity of neurons in behaving mice. In the MEC, we recorded the activity of grid cells—a widely studied group of neurons important for memory and spatial information processing—while mice navigated in a virtual reality environment.

Fig. 1. Schematic overview. (*A*) mPFC and MEC, together with neighboring regions, are situated within deep fissures, presenting challenges to optical access. (*B*) Strategy for cellular-resolution optical access to the mPFC, MEC, and neighboring regions using a right angle microprism inserted into the fissure. The microprism implant is designed for chronic access in behaving animals. Schematic shows two-photon imaging of the mPFC; the approach in other regions is similar. (*C*) Microprism implant placement for the mPFC and MEC. Coronal and sagittal slices adapted from ref. 7.

resolution using the calcium sensor GCaMP. In the MEC we demonstrate that, when mice navigate in virtual reality (VR), imaged neurons exhibit spatial firing fields that match the expected activity of grid cells as revealed by prior electrophysiological measurements of grid cells in real and virtual environments (12, 13).

Results

Microprism Implant Assembly. We designed and implemented an implantable microprism assembly, consisting of a 1.5-mm right angle glass microprism bonded to a circular glass window and a thin, stainless steel tube (Fig. 2*A*). An aluminum coating on the prism hypotenuse enables internal reflection and a dielectric overcoat protects the aluminum coating from degradation within the corrosive, aqueous environment of the brain. Microprism assemblies remained viable for the duration of our experiments (1–3 mo following implantation). When the stainless steel tube is bonded to the skull using dental cement, the tube and glass window provide a permanent seal and a mechanically stable mounting point for the microprism (Fig. 1*B*). The glass window applies a light downward pressure (~200 μm) to reduce brain motion during behavior (11, 14). An implanted titanium headplate allows the head to be held fixed under a microscope during behavior, such as running on a spherical treadmill and navigation in VR (14, 15). Together, the features of the microprism assembly enable chronic, stable optical access in animals engaged in head-fixed behavior.

Microprism Implantation. Anatomical features of the vasculature and meninges surrounding fissures present unique challenges for microprism implantation (Fig. 2 *B* and *C*). The dura consists of two joined layers that separate to form a venous channel, the superior sagittal sinus, which courses over the longitudinal fissure between the cerebral hemispheres. Over the midline, the outer layer of the dura attaches to the inner surface of the skull, and the inner layer folds into the fissure to form the cerebral falx, which separates the hemispheres. A similar dural reflection, the cerebellar tentorium, separates the cortex and cerebellum at the transverse fissure and forms the overlying transverse sinus (16). These dural venous sinuses, together with associated vasculature and the surrounding dura, prevent direct access to the underlying fissures. Furthermore, the superior sagittal and transverse sinuses form one of the major venous outflow systems of the brain,

draining the dorsal cortex and cerebellum in addition to various underlying regions (8). Therefore, in studies of healthy brain function, they should not be resected, and care must be taken to avoid damaging them.

Our surgical procedure addressed these anatomical challenges as follows. Before implantation, we screened and measured the superficial cerebral vasculature of each mouse through a surgically thinned area of the skull over the implantation region. Dorsal cortical and cerebellar veins drain into bridging veins and the sigmoid sinuses, which join with the superior sagittal and transverse sinuses (Fig. 2*B*). Bridging veins and the sigmoid sinuses block local microprism insertion because they span the fissures (Fig. 2*C*), and severing them would cause hemorrhage. Although gross vascular anatomy is conserved across individuals, we found that the location and geometry of bridging veins are variable, as is the location of the sigmoid sinuses. Therefore, in the mPFC, we used vasculature measurements in each individual to choose the implantation hemisphere and to adjust implantation coordinates to avoid bridging veins. We used only mice for which small adjustments (<500 μm) were necessary. In the MEC, we held the implantation site fixed and used only mice in which it was clear of bridging veins and the sigmoid sinuses.

We subsequently performed a craniotomy over the implantation site. Standard craniotomy techniques involve cutting and lifting away a large flap of bone as a single piece. However, we found that this procedure could tear the dural venous sinuses, which are attached to the skull in some locations by the outer dural layer and by emissary veins that connect the sinus with diploic veins within the skull (Fig. 2*C*). Instead, we first thinned a narrow region of the skull over the sinus and removed it as small, individual bone flakes, which could be carefully separated from the underlying tissue and peeled away without causing tears. We then removed the remaining bone over the implantation site and, to gain access to the fissure, created an incision in the dura along the side of the sinus. We removed the dura over
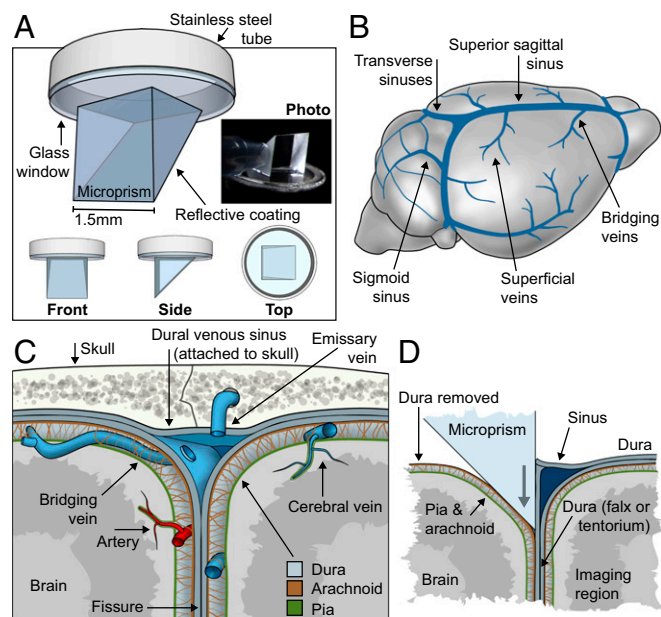
Fig. 2. Microprism implant, anatomy, surgery. (*A*) Microprism implant assembly. Prism hypotenuse is coated with aluminum for internal reflection and a dielectric overcoat for protection against corrosion and abrasion. (*B–D*) Anatomy of the vascular system and meninges, as relevant to microprism implantation into fissures. (*B*) Superficial venous system of the mouse brain. (*C*) Vasculature and meninges surrounding deep fissures. The longitudinal fissure and overlying superior sagittal sinus are shown; the transverse fissure and overlying transverse sinus are similar. (*D*) Insertion of the microprism into the fissure.

www.manaraa.com
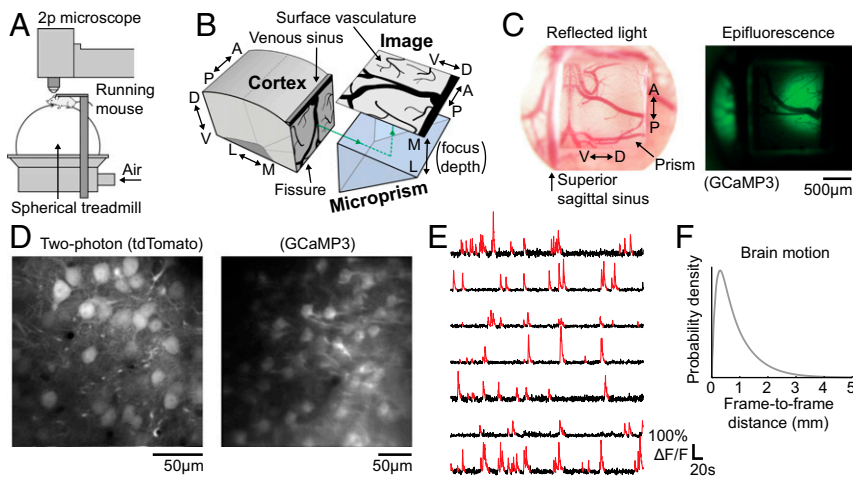
Fig. 3. Imaging the mPFC in behaving mice. (*A*) Experimental set-up: Two-photon imaging of the mPFC in mice running on an air-supported spherical treadmill. (*B*) Image formation through an implanted microprism. A, anterior; D, dorsal; L, lateral; M, medial; P, posterior; V, ventral. (*C*) Widefield images of the mPFC through the implanted microprism. (*Left*) Reflected light image. (*Right*) epifluorescence image of GCaMP3 labeling. (*D*) Two-photon images of mPFC layer 2/3 neurons expressing tdTomato (*Left*) or GCaMP3 (*Right*). (*E*) Somatic calcium dynamics during running behavior. Traces show GCaMP3 fluorescence of simultaneously recorded neurons. Red identifies significant calcium transients, identified with <5% false-positive rate. (*F*) Distribution of the estimated distance the brain moved within the focal plane between successive frames (measured at 13 Hz).

the implantation site so that it would not compress adjacent brain regions during microprism implantation.

We inserted the microprism into the subdural space within the fissure (Fig. 2*D*), which shifted the sinus forward by ~150 μm. Once implanted, the prism sat flush against the opposing fissure wall, which contained the region to image. The brain tissue opposite the prism retained its dural covering, and remained separated from the prism face by the cerebral falx or cerebellar tentorium. The area directly beneath the microprism was compressed, but remained intact.

Using these procedures, we found that 97% of mice (35 of 36) survived the implantation surgery and remained healthy. The mice recovered quickly and displayed no gross impairments or behavioral differences compared with nonimplanted mice. Implanted mice exhibited typical running, climbing, grooming, nest building, sleeping, and foraging behaviors, and maintained a healthy weight and appearance. They also learned to control a spherical treadmill and navigate in virtual environments in a manner comparable to nonimplanted mice.

Imaging the mPFC in Behaving Mice. Using these surgical procedures, we implanted microprisms into the longitudinal fissure and chronically imaged the mPFC in behaving mice (Figs. 1*C* and 3*A*). To optically measure neuronal structure and function, we imaged the fluorescent protein tdTomato or the genetically encoded calcium indicator GCaMP3 (17). Probes were expressed in the mPFC contralateral to the prism by injecting recombinant adeno-associated viral vectors (rAAV) (*SI Materials and Methods*).

In the mPFC, 61% of mice screened (38 total) had bridging vein configurations that allowed implantation within 500 μm of target coordinates. Of the 15 mice that did not satisfy this criterion, 13 had bridging veins coursing over the dorsal cortical surface and were detected at the thinned-skull screening step, and 2 had bridging veins coursing along the medial wall of the cortex, within the fissure.

To obtain a broad view of the tissue through the entire prism and cranial window, we first imaged through a widefield microscope at low magnification (Fig. 3*C*). The brain and vasculature maintained a clear, healthy appearance in reflected light images over the course of our experiments (1–3 mo postimplantation). Robust blood flow was visible in the superior sagittal sinus and nearby veins, indicating proper function of the vascular system. In a small subset of mice, light growth of the dura within the fissure appeared 3 mo postimplantation. However, it did not visibly affect widefield or two-photon image quality. GCaMP3 was expressed over a broad area in the mPFC, visible in epifluorescence images.

As a test bed for imaging at cellular resolution during behavior, we trained mice to run on an air-supported spherical

treadmill while their heads were held fixed under a two-photon microscope (14) (Fig. 3*A*). We imaged mPFC layer 2/3 neurons through the prism using two-photon laser-scanning microscopy while mice freely ran, rested, and groomed on the treadmill. We imaged chronically for up to 3 mo following prism implantation (in tdTomato-expressing mice; 5 wk for GCaMP3). tdTomato- and GCaMP3-labeled neurons were clearly visible (Fig. 3*D*), as were large somatic calcium transients (91 ± 53% Δ*F*/*F*) in GCaMP3-labeled cells (Fig. 3*E*). To capture calcium dynamics and discard any artifactual fluctuations, we identified significant transients that exceeded amplitude and duration thresholds (Fig. 3*E*). Thresholds were selected for each cell such that fewer than
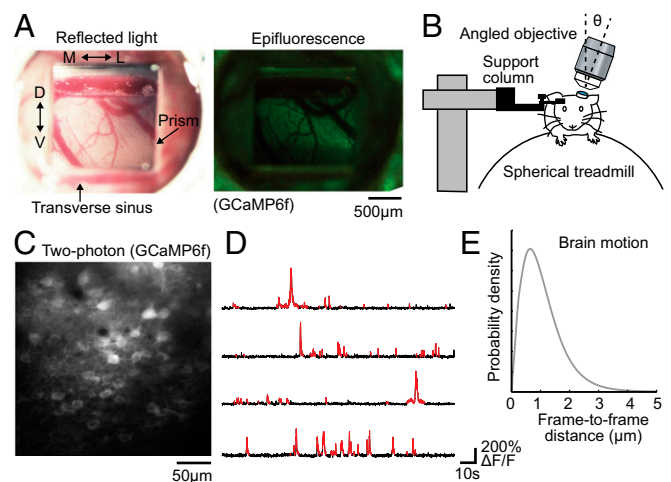
Fig. 4. Chronic imaging of MEC neurons in awake mice. (*A*) Widefield images of the MEC through an implanted microprism. (*Left*) Reflected light image. (*Right*) Epifluorescence image of GCaMP6f labeling. D, dorsal; L, lateral; M, medial; V, ventral. (*B*) Experimental set-up for in vivo imaging of MEC neurons in an awake mouse. The apparatus consists of a spherical treadmill, a support column for attachment of the headplate from a single side, and a two-photon microscope (not shown in detail) with rotatable objective oriented perpendicular to the surface of the prism implant (objective tilt θ: 12–23° from the vertical axis). Mice run freely on the treadmill during imaging. (*C*) In vivo two-photon image of GCaMP6f-labeled cell bodies in layer 2 of the MEC. GCaMP6f is excluded from the nucleus of most cells. (*D*) GCaMP6f fluorescence timecourse from four cells during mouse running behavior. Baseline-subtracted Δ*F*/*F* traces for each cell are shown in black. Significant transients (<5% false-positive rate) are plotted in red. (*E*) Distribution of the estimated distance the brain moved within the focal plane between successive frames, during running behavior.

NEUROSCIENCE
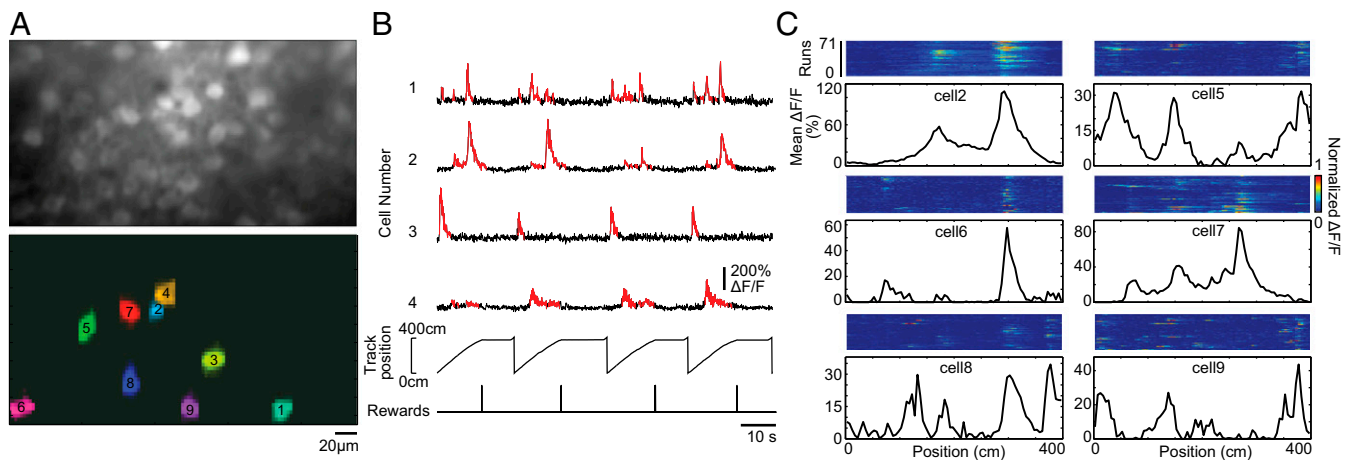
Fig. 5. Imaging of MEC grid cells during virtual navigation. (*A*) Two-photon image of neurons in layer 2 of MEC expressing GCaMP6f. Nine regions of interests defining single cells are shown in different colors (*Lower*). (*B*) GCaMP6f fluorescence traces from four cells during virtual navigation. Baseline-subtracted Δ*F/F* traces are shown in black. Significant transients (<5% false-positive rate) are plotted in red. The position of the mouse along the virtual linear track and water reward timing are shown at the bottom. (*C*) The spatial dependence of calcium transients for six cells in *A*. For each cell (*Top*): heat plot of Δ*F/F* versus linear track position for a set of sequential traversals; (*Bottom*) mean Δ*F/F* versus linear track position, demonstrating calcium transient-based "fields." Cell numbers in *B* and *C* correspond to numbered regions of interest in *A*.

5% of detected transients were expected to arise from spurious sources, such as brain motion orthogonal to the focal plane (14). We quantified in-plane brain motion using the frame displacements estimated by a cross-correlation–based motion-correction algorithm (18) (Fig. 3*F*), which was readily able to compensate for movements and stabilize the images. Brain displacement between consecutive frames at 13 Hz was 0.9 ± 0.7 μm, comparable to previously reported values (18).

Imaging the MEC in Behaving Mice. We further used the methods described above to implant microprisms into the transverse fissure and to chronically image the MEC in behaving mice. A fixed set of implantation coordinates provided broad coverage of the MEC along the mediolateral axis (the prism spanned from 2.6 to 4.0 mm lateral of the midline). We selectively implanted the left hemisphere because it tended to contain fewer visible blood vessels near the implantation site (*SI Materials and Methods*). Vasculature allowed implantation in 76.3% of mice when this strategy was followed.

The chronically implanted microprism allowed one- and two-photon imaging of the MEC for up to 2 mo (Fig. 4 *A* and *C*) in 13 of 14 mice; in one mouse, dural regrowth reduced imaging quality 1 mo postimplantation. We measured activity-related changes in intracellular calcium concentration using the genetically encoded calcium indicator GCaMP6f (19), expressed in layer 2 and 3 neurons in the dorsal MEC using an rAAV vector (Fig. 4*A* and Fig. S1).

Two-photon imaging of MEC layer 2 neurons was performed in mice running on a spherical treadmill (14) (Fig. 4*B*). To provide clearance for the cranial window and microscope objective, mice were head-fixed using a support column located on their right side, and an implanted headplate with a single support arm. The headplate and the microscope's rotatable objective were positioned with an appropriate relative angle so that the surface of the cranial window was parallel to the focal plane of the objective, reducing optical aberrations. After mice were trained to run on the spherical treadmill, GCAMP6f-expressing neurons in MEC layer 2 were routinely imaged during free running behavior (Fig. 4*C*). To detect calcium-related fluorescence changes and discard any motion-induced fluctuations, significant transients were identified within fluorescence time series, with a false-positive rate less than 5% (14). Many cells exhibited fast somatic calcium transients (Fig. 4*D*) (mean transient duration = 1.0 ± 0.9 s) with variable amplitude (peak Δ*F/F* = $128 \pm 121\%$), consistent with the summation of multiple

transients generated by varying numbers of action potentials (17–19). Brain motion (1.1 ± 0.7-μm displacement between consecutive frames at 13 Hz) was comparable to previously reported values (18) and was readily correctable in software.

Imaging the MEC During Navigation in Virtual Reality. Previous electrophysiological recordings have shown that grid cells in the MEC exhibit spatial firing fields when animals traverse linear tracks in physical or VR environments (12, 13, 20). To optically characterize grid cell activity, we imaged the MEC through an implanted microprism while mice navigated in a VR environment, which was projected onto a toroidal screen and controlled using the spherical treadmill (15, 18) (Fig. S2*A*). Mice were trained to navigate in one direction along a 400-cm-long linear track for a water reward at the end, followed by teleportation back to the beginning (Fig. S2*B*). The track environment and unidirectional navigation behavior were similar to those previously used for whole-cell recordings of grid cells in VR (12).

Fields of view (FOVs) in layer 2 of the dorsal MEC were imaged for 20–35 min each, during which mice traversed the track one to three times per minute. Many cells exhibited statistically significant calcium transients during VR navigation (Fig. 5 *A* and *B*), and multiple responding cells could be simultaneously recorded. Calcium dynamics during navigation were often spatially modulated; transients occurred reliably as a function of the mouse's position along the track, with localized peaks in intensity (i.e., "fields") at one or more track positions (Fig. 5*C*).

Spatial calcium response patterns with multiple fields (Fig. 5*C*) resembled the electrophysiologically measured firing fields of grid cells along similar linear tracks (12, 13, 20) (Fig. S3), and had similar shape, field spacing, and number of fields. Importantly, for all six simultaneously recorded cells in Fig. 5*C* (intersomatic distance 101 ± 42 μm), spatial calcium transient fields along the linear track were well approximated by slices through 2D hexagonal grid lattices (Fig. S4). The best-fit lattices had similar grid spacing (69.7 ± 2.4 cm), field width (48.2 ± 3.7 cm), and slice angles ($21.1 \pm 1.7°$) across cells. These properties are consistent with those observed in electrophysiologically recorded grid cells in close proximity to each other. Such cells typically share similar field spacing and width during navigation in 2D arenas. Furthermore, their firing fields along a linear track resemble slices through a 2D hexagonal grid lattice, with similar slice angles across cells (4, 12, 21, 22).

Low et al.

Our combined microprism/VR method facilitates large-scale recording of the spatial patterning of neural activity in the MEC. In a typical 180 × 360-μm FOV containing 80–100 GCaMP6f-labeled cells in layer 2, we were able to simultaneously record 20–60 cells with spatially modulated activity (varying with FOV location) (Fig. S5). To begin to characterize the spatial field properties of optically recorded cells, we calculated the field spacing and field width of each neuron from the spatial autocorrelation function of its mean calcium transient activity along the track (Fig. S6) (12, 13). Cells showed increased field spacing from dorsal to ventral FOVs (Fig. 6 and Figs. S7 and S8) (most dorsal FOV, 154 ± 17 cm; most ventral FOV, 260 ± 15 cm, mean ± SEM). In parallel, the field width increased from 94 ± 10 cm in the most dorsal FOV to 150 ± 10 cm in the most ventral FOV. This gradual increase in field width and spacing along the dorsoventral axis of the MEC is a well-established property of grid cells (4, 5, 13, 21, 22).

Discussion

We developed a strategy for in vivo, cellular resolution optical access to brain regions enclosed within deep fissures. Key components included a microprism-based cranial window implant and surgical procedures for implanting it into the longitudinal or transverse fissure. Combining optical access to fissures with the genetically encoded calcium indicator GCaMP (17, 19) and methods for two-photon imaging in behaving mice (14), we chronically imaged neuronal activity in the mPFC and MEC, two brain areas that have not previously been accessible to cellular-resolution imaging. Brain motion in both regions during running behavior was on the micron scale, comparable to motion in dorsal mouse brain regions imaged with conventional implants. Because of this high stability, statistically significant calcium transients could be optically recorded from populations of GCaMP-expressing neurons during running behavior.

Although the roles of the mPFC and MEC in learning, memory, decision making, and spatial representation have been studied using electrophysiological methods (23–26), cellular resolution optical access to these areas has been challenging because they are folded within the walls of fissures, and major regions are located beyond 500 μm deep below the dorsal brain surface. Existing in vivo two-photon imaging methods are more efficient in imaging superficial areas (<500 μm) because of scattering and out-of-plane fluorescence excitation (27–30). Although several approaches have been developed to image deeper tissues using two-photon excitation with longer wavelengths (31–33) or higher peak pulse power (34, 35), their properties have so far limited their applications in the functional imaging of the mPFC and MEC. Aspiration of overlying cortical tissue has been used to optically access hippocampal neurons (18). However, the mPFC and MEC localize under the superior sagittal and transverse sinuses, respectively, which are crucial for cerebral drainage. The importance of these sinuses prevents aspiration of the tissue directly above the mPFC and MEC. Although blunt-ended gradient index (GRIN) lenses have also been applied to image the hippocampus and many deep brain regions (36, 37), the use of GRIN lenses was limited by their optical aberrations, relatively small FOV for two-photon imaging, and short working distances. Moreover, the geometry of the mPFC or MEC would require that GRIN lenses penetrate through cortical columns or the cerebellum, with the potential for interfering with brain function.

Our approach has its origin in a different category of deep brain imaging methods using right-angle microprisms. A 0.5-mm prism has been previously used in a fiberoptic periscope, enabling one-photon recording of calcium activity of layer 5 pyramidal cell dendrites (9). More recently, a 1-mm prism allowed acute and chronic imaging of deep layers in dorsal cortical regions (10, 11). Using two-photon microscopy, neuronal morphology and calcium transients were successfully recorded across all six cortical layers (400–600 μm thick) in a single FOV. The imaging depth perpendicular to the prism surface was >100–
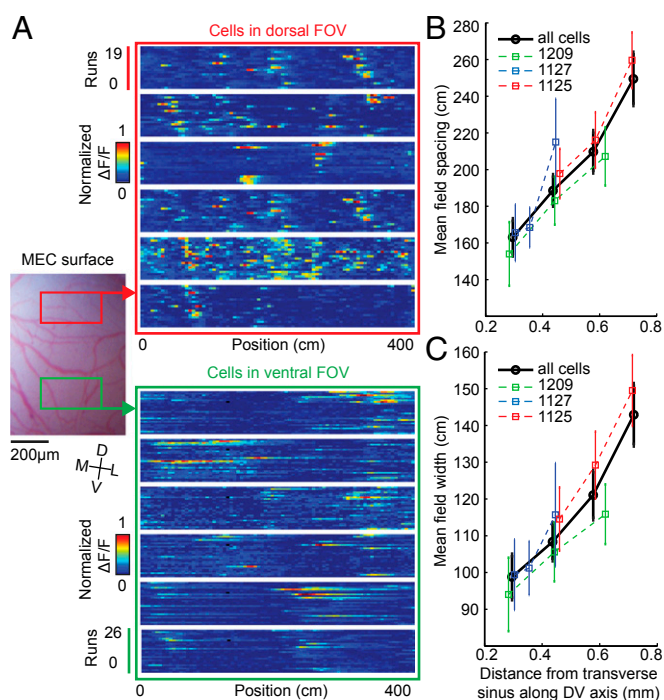
Fig. 6. Field spacing and width increase along the dorso-ventral (D-V) axis of the MEC. (*A*) Spatial patterning of calcium transients with track position from cells in two imaging FOVs along the D-V axis of MEC. FOVs (*Left*) are outlined in magenta (dorsal FOV) and green (ventral FOV) on a widefield MEC image. (*Right Upper*) (red box): calcium transient-based fields of six simultaneously recorded cells in the dorsal FOV. For each cell, ΔF/F versus linear track position is plotted as a heat map for a set of traversals along a 400-cm track. (*Right Lower*) (green box): calcium transient fields of six simultaneously recorded cells in the ventral FOV. (*B*) Population analysis showing the dependence of field spacing on dorsal to ventral MEC location. An individual cell's field spacing was calculated from its spatial autocorrelation function as the distance between the peak at 0 cm and the first local maximum (Fig. S6). Each colored curve represents data from one mouse. Each datapoint represents (mean ± SEM) field spacing from 17 to 50 simultaneously recorded cells in a single FOV; the mean distance from transverse sinus along the D-V axis of all cells in the FOV was used as the distance along the D-V axis. The black curve represents field spacing of all cells from the three mice. Cells were sorted in four equally spaced bins based on their physical distance from the transverse sinus along the D-V axis. Each datapoint represents (mean ± SEM) field spacing from cells in each bin. Bin center was used as the distance along the D-V axis. (*C*) Population analysis showing the dependence of field width on the dorsal to ventral MEC location of imaged cells. The field width of each cell was calculated as the width of central peak of the autocorrelation function. Each colored curve represents data from one mouse. Each datapoint represents (mean ± SEM) field width from simultaneously recorded cells in a single FOV (FOVs are the same as in *B*); the mean distance from transverse sinus along D-V axis of all cells in the FOV was used as the distance along the D-V axis. The black curve represents field width of all cells from the three mice. Cells were sorted as described in *B*. Each datapoint represents (mean ± SEM) field width from cells in each bin. Bin center was used as the distance along the D-V axis.

150 μm (11). This method is based on directly inserting the prism into the cortical tissue, however, which may damage the circuitry of the mPFC, MEC, and other regions along fissure walls, given their folded geometry (23, 38). Our method extends this prior art in microprism-based imaging by adding the new capability for imaging within fissures.

When combined with virtual reality for head-restrained mice (15, 18), the optical access provided by a microprism inserted into the transverse fissure enabled functional imaging of the MEC in mice navigating along a linear track. Many layer 2 neurons in the dorsal MEC had spatially localized activity,

Low et al.

NEUROSCIENCE

www.manaraa.com

consisting of calcium transients that occurred reliably at one or more positions along the track (Figs. 5 and 6 and Fig. S5). We termed these regions "calcium transient fields" in analogy with the action potential firing fields of grid cells recorded with electrodes. Several lines of evidence support the conclusion that these optically recorded cells contained a population of grid cells. First, calcium transient fields had spacing and amplitude patterns that were qualitatively similar to those of grid cell firing fields measured electrophysiologically along linear tracks (12, 13, 20). Moreover, many optically measured fields could be placed into direct correspondence with previous tetrode and whole-cell recordings of grid cells in a nearly identical VR environment (12) (Fig. S3). Second, calcium transient fields along the linear track were well approximated as slices through hexagonal lattices modeling 2D grid cell firing fields (Fig. S4). For the six simul-taneously imaged cells shown in Fig. 5, the best-fit lattices had similar field widths and spacing. All six cells had similar slice angles relative to the lattices, and their different activity patterns corresponded to different offsets of the slice within the lattice. These features are consistent with the properties of electrode-recorded grid cells in the MEC, in that nearby grid cells typically have similar field spacing and widths in 2D arenas, and similar slice angles through a model 2D grid lattice during navigation along a 1D track (4, 12, 21). Finally, in a population analysis based on the spatial autocorrelation, imaged MEC neurons exhibited increased field spacing and width from dorsal to ven-tral cell body locations within layer 2 (Fig. 6 and Figs. S7 and S8). This correlation between the field patterns and anatomical lo-cation is a feature of electrophysiologically recorded grid cells, which show a progressive increase in grid field spacing and width along the dorsoventral axis of the MEC (4, 5, 13, 21, 22). The spacing of calcium transient fields along the track was compa-rable in scale to electrophysiologically measured grid cell firing fields along real and virtual linear tracks (13). Although calcium

transient field widths were slightly expanded in comparison with electrophysiologically recorded grid field widths in the same virtual environment (13), this broadening is an expected consequence of the dynamics of calcium indicators and intracellular calcium (18, 19). Overall, these features of the calcium transient fields of the MEC layer 2 cells are consistent with the properties of grid cells recorded by electrophysiological methods, strongly suggesting that we imaged grid cells in layer 2 of the MEC.

We have demonstrated chronic imaging of neuronal activity in the mPFC and MEC during behavior, and of the MEC grid cell network during spatial navigation. These widely studied struc-tures were not previously accessible using high-resolution optical techniques. By providing optical access to deep fissures, the methods presented herein open up these structures for study at cellular resolution in behaving animals using the powerful, rap-idly expanding palette of optical tools for perturbing and measuring network structure and function (39, 40). Finally, with further optimization, our current method can be used to image not only the mPFC and MEC, but also other brain regions within fissures, such as the parasubiculum and retro-splenial granular cortex.

Materials and Methods

All animal experiments were performed with approval of the Princeton University Institutional Animal Care and Use Committee. Mice used were adult C57BL/6 males. Microprism implant construction, surgical procedures, imaging, behavior, data analysis, and histology are described in *SI Materials and Methods*.

1. Yuste R (2011) *Imaging: A Laboratory Manual* (Cold Spring Harbor Lab Press, Cold Spring Harbor, N.Y.), xvi pp.
2. Fuster JM (2001) The prefrontal cortex—An update: Time is of the essence. *Neuron* 30(2):319–333.
3. Goldman-Rakic PS (1995) Cellular basis of working memory. *Neuron* 14(3):477–485.
4. Hafting T, Fyhn M, Molden S, Moser MB, Moser EI (2005) Microstructure of a spatial map in the entorhinal cortex. *Nature* 436(7052):801–806.
5. Fyhn M, Molden S, Witter MP, Moser EI, Moser MB (2004) Spatial representation in the entorhinal cortex. *Science* 305(5688):1258–1264.
6. Theer P, Denk W (2006) On the fundamental imaging-depth limit in two-photon microscopy. *J Opt Soc Am A Opt Image Sci Vis* 23(12):3139–3149.
7. Paxinos G, Franklin KBJ (2001) *The Mouse Brain in Stereotaxic Coordinates* (Academic, San Diego), 2nd Ed.
8. Scremin OU, Holschneider DP (2012) Vascular supply. *The Mouse Nervous System*, eds Watson C, Paxinos G, Puelles L (Elsevier Academic, Amsterdam), pp 459–472.
9. Murayama M, Pérez-Garci E, Lüscher HR, Larkum ME (2007) Fiberoptic system for recording dendritic calcium signals in layer 5 neocortical pyramidal cells in freely moving rats. *J Neurophysiol* 98(3):1791–1805.
10. Chia TH, Levene MJ (2009) Microprisms for in vivo multilayer cortical imaging. *J Neurophysiol* 102(2):1310–1314.
11. Andermann ML, et al. (2013) Chronic cellular imaging of entire cortical columns in awake mice using microprisms. *Neuron* 80(4):900–913.
12. Domnisoru C, Kinkhabwala AA, Tank DW (2013) Membrane potential dynamics of grid cells. *Nature* 495(7440):199–204.
13. Brun VH, et al. (2008) Progressive increase in grid scale from dorsal to ventral medial entorhinal cortex. *Hippocampus* 18(12):1200–1212.
14. Dombeck DA, Khabbaz AN, Collman F, Adelman TL, Tank DW (2007) Imaging large-scale neural activity with cellular resolution in awake, mobile mice. *Neuron* 56(1):43–57.
15. Harvey CD, Collman F, Dombeck DA, Tank DW (2009) Intracellular dynamics of hip-pocampal place cells during virtual navigation. *Nature* 461(7266):941–946.
16. Mendoza JE, Foundas AL (2007) *Clinical Neuroanatomy: A Neurobehavioral Approach* (Springer, New York), pp ix.
17. Tian L, et al. (2009) Imaging neural activity in worms, flies and mice with improved GCaMP calcium indicators. *Nat Methods* 6(12):875–881.
18. Dombeck DA, Harvey CD, Tian L, Looger LL, Tank DW (2010) Functional imaging of hippocampal place cells at cellular resolution during virtual navigation. *Nat Neurosci* 13(11):1433–1440.
19. Chen TW, et al. (2013) Ultrasensitive fluorescent proteins for imaging neuronal ac-tivity. *Nature* 499(7458):295–300.
20. Hafting T, Fyhn M, Bonnevie T, Moser MB, Moser EI (2008) Hippocampus-independent phase precession in entorhinal grid cells. *Nature* 453(7199):1248–1252.
21. Fyhn M, Hafting T, Witter MP, Moser EI, Moser MB (2008) Grid cells in mice. *Hippo-campus* 18(12):1230–1238.
22. Stensola H, et al. (2012) The entorhinal grid map is discretized. *Nature* 492(7427):72–78.
23. Euston DR, Gruber AJ, McNaughton BL (2012) The role of medial prefrontal cortex in memory and decision making. *Neuron* 76(6):1057–1070.
24. Moser EI, et al. (2014) Grid cells and cortical representation. *Nat Rev Neurosci* 15(7):466–481.
25. Takehara-Nishiuchi K (2014) Entorhinal cortex and consolidated memory. *Neurosci Res* 84C:27–33.
26. Fujisawa S, Buzsáki G (2011) A 4 Hz oscillation adaptively synchronizes prefrontal, VTA, and hippocampal activities. *Neuron* 72(1):153–165.
27. Svoboda K, Yasuda R (2006) Principles of two-photon excitation microscopy and its applications to neuroscience. *Neuron* 50(6):823–839.
28. Centonze VE, White JG (1998) Multiphoton excitation provides optical sections from deeper within scattering specimens than confocal imaging. *Biophys J* 75(4):2015–2024.
29. Denk W, et al. (1994) Anatomical and functional imaging of neurons using 2-photon laser scanning microscopy. *J Neurosci Methods* 54(2):151–162.
30. Zinter JP, Levene MJ (2011) Maximizing fluorescence collection efficiency in multi-photon microscopy. *Opt Express* 19(16):15348–15362.
31. Horton NG, et al. (2013) In vivo three-photon microscopy of subcortical structures within an intact mouse brain. *Nat Photonics* 7(3):205–209.
32. Kobat D, Horton NG, Xu C (2011) In vivo two-photon microscopy to 1.6-mm depth in mouse cortex. *J Biomed Opt* 16(10):106014.
33. Kawakami R, et al. (2013) Visualizing hippocampal neurons with in vivo two-photon microscopy using a 1030 nm picosecond pulse laser. *Sci Rep* 3:1014.
34. Mittmann W, et al. (2011) Two-photon calcium imaging of evoked activity from L5 somatosensory neurons in vivo. *Nature neuroscience* 14(8):1089–1093.
35. Theer P, Hasan MT, Denk W (2003) Two-photon imaging to a depth of 1000 microm in living brains by use of a Ti:Al2O3 regenerative amplifier. *Optics letters* 28(12):1022–1024.
36. Barretto RP, et al. (2011) Time-lapse imaging of disease progression in deep brain areas using fluorescence microendoscopy. *Nat Med* 17(2):223–228.
37. Jung JC, Mehta AD, Aksay E, Stepnoski R, Schnitzer MJ (2004) In vivo mammalian brain imaging using one- and two-photon fluorescence microendoscopy. *J Neurophysiol* 92(5):3121–3133.
38. Canto CB, Wouterlood FG, Witter MP (2008) What does the anatomical organization of the entorhinal cortex tell us? *Neural Plast* 2008:381243.
39. Nikolenko V, Poskanzer KE, Yuste R (2007) Two-photon photostimulation and im-aging of neural circuits. *Nat Methods* 4(11):943–950.
40. Rickgauer JP, Deisseroth K, Tank DW (2014) Simultaneous cellular resolution optical pertur-bation and imaging of hippocampal place cell firing fields. *Nat Neurosci* 17(12):1816–1824.

www.manaraa.com